Finite-Set Model Predictive Power Control of Brushless Doubly Fed Twin Stator Induction Generator

Xinchi Wei, *Student Member, IEEE*, Ming Cheng, *Fellow, IEEE*, Jianguo Zhu, *Senior Member, IEEE*, Haitao Yang, *Student Member, IEEE*, and Rensong Luo

***Abstract*—This paper presents a finite-set model predictive power control (FS-MPPC) method for the brushless doubly fed twin stator induction generator (BDFTSIG) in variable speed constant frequency generation applications. The FS-MPPC controller is developed in a general reference frame from which all other reference frames can be deduced readily. The invariant feature of the predictive power model in various reference frames contributes to the reference frame-free characteristic of the developed FS-MPPC controller, enabling its application more flexible and universal. Besides, the arduous process of control winding flux estimation is avoided in the FS-MPPC controller by choosing state variables that are easy to be obtained. Moreover, the influence of rotor circuit that has long been neglected in the existing controllers for the brushless doubly fed induction machines is embedded within the predictive power model and inherently considered in the FS-MPPC controller, which contributes to accurate power control of the BDFTSIG. Furthermore, the feasibility and effectiveness of the developed FS-MPPC controller regarding different power levels and grid fault conditions are briefly discussed. Finally, numerical simulations and experimental tests are carried out, which demonstrates the effectiveness of the developed FS-MPPC controller.**

***Index Terms*—Brushless doubly fed twin stator induction generator (BDFTSIG), model predictive power control, variable speed constant frequency (VSCF) generation.**

NOMENCLATURE

A. Main Variables

f Frequency (Hz).
i Instantaneous current (A).

Manuscript received December 6, 2017; revised April 14, 2018; accepted May 28, 2018. Date of publication June 6, 2018; date of current version February 5, 2019. This work was supported by the National Natural Science Foundation of China under Project 51320105002. Recommended for publication by Associate Editor J. Rodriguez. *(Corresponding author: Ming Cheng.)*

X. Wei and M. Cheng are with the School of Electrical Engineering, Southeast University, Nanjing 210096, China (e-mail:

However, the operating principle of BDFIM is far more complex than that of DFIM, and the corresponding control technology needs to be intensively investigated to facilitate the development of BDFIMs.

Researchers have exerted tremendous effort in the control of BDFIMs, starting from open-loop control [7] and closed-loop scalar control [8], and then focusing on various vector control (VC) methods [9]–[15] for stable operation and decoupled control. Hopfensperger *et al.* [9], Basic *et al.* [10], and Shao *et al.* [11] clearly present the basic control structure in stator flux oriented frame. In [9], the dq coupling brought by the specialized closed rotor circuit in BDFIM are first introduced, and the influence of operation speed and rotor resistance on the dq coupling is analyzed. In [10], complex transfer function method is adopted in dynamic modeling, and the influence of operation speed and rotor transient time constant on transient performance of power control loop is examined theoretically and experimentally. In [11], the control of speed and reactive power is investigated, and the controller is simplified by regarding the high-order items as low-frequency disturbances. In [12], an integral sliding mode control method is incorporated into the vector control frame to guarantee the speed tracking performance. In [13] and [14], standalone operation of BDFIM and the corresponding controller design are studied. In [13], a direct voltage control method developed in inner stator current oriented frame is presented for simple, robust and cost-effective operation. In [14], the BDFIM and the load are modeled as a dual-input-dual-output system by the DN method, based on which the inner current controller is designed to obtain good decoupling feature. In [15], an improved vector controller based on single synchronous reference frame is proposed for BDFIM under unbalanced grid conditions by introducing PI+R controller. In these well-developed VC methods, appropriate reference frame has to be determined first and usually cascaded control structure in combination with a modulation step is adopted. Besides, much tuning work is required to ensure the system stability over the whole operating range. In addition, the influence of rotor circuit, which results in coupling terms or asynchronous torque, has been neglected in the implementation of the existing VC controllers.

Recently, nonlinear direct control methods such as direct torque control (DTC) method and direct power control (DPC) method, which can overcome the large tuning work and reduce the control complexity in VC methods, have been applied to the control of BDFIMs [16]–[21]. In [16], a classical DTC strategy is implemented for BDFIM, and it is detected that the complete control of torque and flux is not assured in the entire sector. Then two different control solutions are proposed to consider "flux priority" and "torque priority," respectively. In [17], a DPC strategy is developed for BDFIM to improve the power quality under unbalanced grid condition. By adding power compensation terms in power references, the negative sequence components of the power machine stator currents can be eliminated, and the power quality is improved. In [18], DPC strategy is combined with maximum power point tracking [19] for open-winding brushless doubly fed reluctance generator in wind energy conversion application. In [20], direct virtual torque is applied in the grid synchronization process of BDFIM, which can provide fast grid synchronization. In [21], a comprehensive comparison between VC and DTC for BDFIM is carried out. Although these methods can achieve desired dynamic performance, the influence of rotor circuit is omitted in design of the switching table by neglecting the rotor resistance/flux. Besides, the voltage vector selected from the predefined looking up table in DPC/DTC method is not necessarily the best one, and the main drawback of this method is large ripples in power/torque. Moreover, a CW flux observer is required, which is an arduous process in the control of BDFIMs because the frequency of CW flux is low, and its observer is sensitive to parameter mismatches, dc offset, dead-time of the PWM converter, etc. Therefore, it is necessary to develop some novel control schemes to address the challenges of accurate power/torque control of BDFIMs with fast dynamic response.

Model predictive control (MPC) has been widely researched for high performance control of electrical machines and power electronic systems, and finite-set model predictive control (FS-MPC) is regarded as a promising form of MPC [22]. The FS-MPC method evaluates the finite-set of possible switching states of the power converter, and then selects the state that optimizes the defined cost function. It can achieve fast dynamic response by avoiding the cascaded control structure and the modulation step. It is also possible to take advantage of the discrete nature of power converters and consider the nonlinearities of motor drives [22]–[28].

This paper investigates the brushless doubly fed twin stator induction generator (BDFTSIG) in applications of VSCF generation systems. The BDFTSIG consists of two cascaded induction machines, magnetically and electrically insulated, with common shaft and interconnected rotor [10], [29], [30]. The first stator winding directly connected to the power system grid is termed as power winding (PW), while the second stator winding supplied from a controlled voltage or current source of variable frequency is termed as control winding (CW). The closed-loop rotor winding probably formulated by two sets of windings is represented by rotor winding (RW).

A finite-set model predictive power control (FS-MPPC) method is proposed for the BDFTSIG. A preliminary study has been carried out in [31], but only a few simulation results were presented. This paper develops the predictive power model and the FS-MPPC controller in a general form that is more flexible and universal. Besides, the implementation of the proposed FS-MPPC controller is clearly described. In addition, more numerical simulations considering various reference frames, different power levels, and grid fault conditions are performed to comprehensively demonstrate the characteristics of the developed FS-MPPC controller. Furthermore, the performance of the developed FS-MPPC controller is compared with an improved and well-tuned vector controller, which clearly reveals the superiority of the developed controller in dynamic performance. Finally, the effectiveness of the developed FS-MPPC controller is further validated by the experimental tests carried out on a prototype BDFTSIG system. The main contribution of this paper includes

1) Predictive power model of the BDFTISIG, which clearly reveals the relationship between the input voltage vector and the future power behavior, is derived for the first time.

2) PW current, CW current, and PW flux, which are easy to be measured or estimated, are chosen as state variables. The CW flux observer that is required in DPC/DTC controllers is not needed in the developed FS-MPPC controller, which facilitates the implementation by avoiding the estimation of low-frequency flux.
3) The influence of rotor circuit that has long been neglected in both VC and DTC/DPC controllers is embedded within the predictive power model and inherently considered in the developed FS-MPPC controller, which contributes to accurate power control of the BDFTSIG.
4) Unlike the VC controllers in which an appropriate reference frame has to be determined first, the developed FS-MPPC controller is not restricted to a specific reference frame. This reference frame-free feature contributes to high flexibility and universality.
5) Unlike the VC controllers in which the controller parameters need to be retuned regarding different systems. Parameter tuning is not required in the FS-MPPC controller, and the developed controller has been demonstrated to be feasible for BDFTISIG systems rated at different power levels.
6) The feasibility and effectiveness of the developed FS-MPPC controller under grid fault conditions are validated and briefly discussed.

II. Dynamic Model of the BDFTSIG

The dynamic voltage equations of the BDFTSIG can be expressed in the general reference frame as [30]

$$[\boldsymbol{v}^g] = [Z^g][\boldsymbol{i}^g] \tag{1}$$

where

$$[\boldsymbol{v}^g] = \begin{bmatrix} \boldsymbol{v}_{ps}^g \\ (\boldsymbol{v}_{cs}^g e^{j\theta_h})^* \\ 0 \end{bmatrix}, [\boldsymbol{i}^g] = \begin{bmatrix} \boldsymbol{i}_{ps}^g \\ (\boldsymbol{i}_{cs}^g e^{j\theta_h})^* \\ \boldsymbol{i}_r^g \end{bmatrix}, [Z^g] =$$

$$\begin{bmatrix} R_{ps}+(s+j\omega_g)L_{ps} & 0 & (s+j\omega_g)L_{pM} \\ 0 & R_{cs}+(s+j\omega_c)L_{cs} & -(s+j\omega_c)L_{cM} \\ (s+j\omega_r)L_{pM} & -(s+j\omega_r)L_{cM} & R_r+(s+j\omega_r)L_r \end{bmatrix}$$

$\omega_c = \omega_g - p_p\omega_m - p_c\omega_m, \omega_r = \omega_g - p_p\omega_m$. θ_h is the transformation angle that maps the CW-side space vectors on to the same reference frame as the PW-side space vectors.

Equation (1) reveals the direct relationship between current and voltage, and it can also be written in a form considering flux linkages as intermediate variables. The flux linkages are depicted in Fig. 1, in which $\boldsymbol{\psi}_r^g$ is the combined rotor flux linkage.

The flux linkages in the general reference frame are formulated as

$$\boldsymbol{\psi}_{ps}^g = L_{ps}\boldsymbol{i}_{ps}^g + L_{pM}\boldsymbol{i}_r^g \tag{2}$$

$$\left(\boldsymbol{\psi}_{cs}^g e^{j\theta_h}\right)^* = L_{cs}\left(\boldsymbol{i}_{cs}^g e^{j\theta_h}\right)^* - L_{cM}\boldsymbol{i}_r^g \tag{3}$$

$$\boldsymbol{\psi}_r^g = L_{pM}\boldsymbol{i}_{ps}^g + L_r\boldsymbol{i}_r^g - L_{cM}\left(\boldsymbol{i}_{cs}^g e^{j\theta_h}\right)^* \tag{4}$$

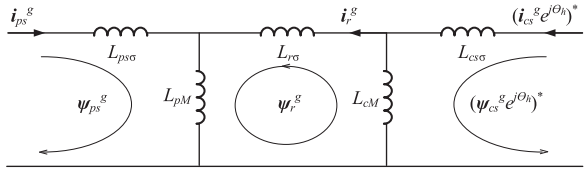

Fig. 1. Flux linkages in the BDFTSIG.

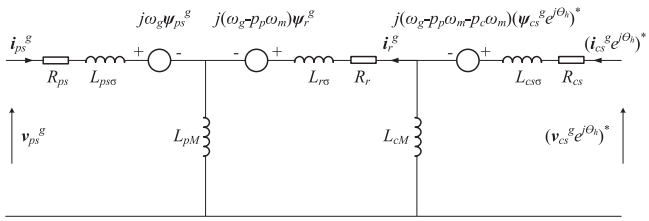

Fig. 2. Equivalent circuit of the BDFTSIG in the general reference frame.

TABLE I
Electrical Frequencies in Various Reference Frames

Reference frame	Electrical frequency (rad/s)
PW stationary frame (PWF)	$\omega^g = \omega_p$
CW stationary frame (CWF)	$\omega^g = \omega_p - p_p\omega_m - p_c\omega_m$
RW stationary frame (RWF)	$\omega^g = \omega_p - p_p\omega_m$
PW synchronous frame (SF)	$\omega^g = 0$

where $L_{ps} = L_{pM} + L_{ps\sigma}, L_{cs} = L_{cM} + L_{cs\sigma}, L_r = L_{pM} + L_{cM} + L_{r\sigma}$.

Finally, the dynamic voltage equations of the BDFTSIG can be written in terms of flux linkages as

$$\boldsymbol{v}_{ps}^g = R_{ps}\boldsymbol{i}_{ps}^g + s\boldsymbol{\psi}_{ps}^g + j\omega_g\boldsymbol{\psi}_{ps}^g \tag{5}$$

$$\left(\boldsymbol{v}_{cs}^g e^{j\theta_h}\right)^* = R_{cs}\left(\boldsymbol{i}_{cs}^g e^{j\theta_h}\right)^* + s\left(\boldsymbol{\psi}_{cs}^g e^{j\theta_h}\right)^* + j\omega_c\left(\boldsymbol{\psi}_{cs}^g e^{j\theta_h}\right)^* \tag{6}$$

$$0 = R_r\boldsymbol{i}_r^g + s\boldsymbol{\psi}_r^g + j\omega_r\boldsymbol{\psi}_r^g. \tag{7}$$

The equivalent circuit in Fig. 2 represents the voltage equations of the BDFTSIG in the general reference frame. In Fig. 2, ω_g represents the instantaneous angular velocity of the general reference frame. When ω_g equals to $0, (p_p + p_c)\omega_m, p_p\omega_m$, and ω_p, the general reference frame is referred to PW stationary frame (PWF), CW stationary frame (CWF), RW stationary frame (RWF), and PW synchronous frame (SF), respectively. If the BDFTSIG is operated in the expected synchronous mode, all the electrical quantities in the general reference frame share the same frequency $(\omega^g = \omega_p - \omega_g)$ which can be summarized in Table I.

It can be observed from Fig. 2 that, due to the closed rotor circuit, the equivalent circuit of BDFIM is much more complicated than that of DFIM. As being revealed in [9], the closed rotor circuit introduces cross-coupling between dq axes, and the larger the rotor resistance, the larger the cross-coupling effect. Therefore, for the wound-rotor BDFIM that has relatively large

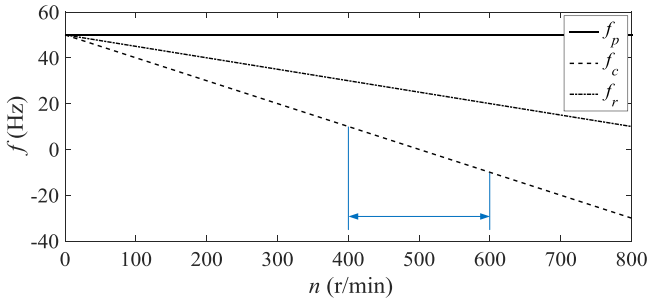

Fig. 3. Frequencies of PW, CW, and RW currents in the BDFTSIG.

rotor resistance, it is necessary to consider the influence of rotor circuit in controller implementation.

III. Predictive Power Model of the BDFTSIG

For clear and concise derivation, the predictive power model of the BDFTSIG is developed in form of complex power, and the corresponding active power and reactive power can be easily obtained by decomposing the real and imaginary components of the complex power. All the derivations are executed in the general reference frame and can be easily transferred to other reference frames.

A. State Space Equations

From flux equations (2)–(4), the currents of PW, CW, and RW can be obtained as

$$\begin{bmatrix} \boldsymbol{i}_{ps}^{g} \\ \boldsymbol{i}_{r}^{g} \\ \left(\boldsymbol{i}_{cs}^{g} e^{j\theta_h}\right)^* \end{bmatrix} = \lambda \begin{bmatrix} L_{cs}L_r - L_{cM}^2 & -L_{cs}L_{pM} & -L_{pM}L_{cM} \\ -L_{cs}L_{pM} & L_{ps}L_{cs} & L_{ps}L_{cM} \\ -L_{pM}L_{cM} & L_{ps}L_{cM} & L_{ps}L_r - L_{pM}^2 \end{bmatrix} \begin{bmatrix} \boldsymbol{\psi}_{ps}^{g} \\ \boldsymbol{\psi}_{r}^{g} \\ \left(\boldsymbol{\psi}_{cs}^{g} e^{j\theta_h}\right)^* \end{bmatrix} \tag{8}$$

where $\lambda = 1/(L_{ps}L_{cs}L_r - L_{ps}L_{cM}^2 - L_{cs}L_{pM}^2)$.

The frequencies of PW, CW, and RW currents are depicted in Fig. 3, taking 3/3 pole-pair combination as an example. The frequency of PW current f_p is constant at 50 Hz, the frequency of RW current f_r is determined by mechanical speed n and f_p, and the frequency of CW current f_c is controlled to satisfy its relationship between f_p and f_r for synchronous operation of the BDFTSIG. The operation range of the BDFTSIG (3/3 pole-pair combination) is usually between 400 r/min and 600 r/min ($\pm$20% natural synchronous speed).

It is obviously observed from Fig. 3 that the maximum value of f_c is 10 Hz during the normal speed range, which makes the implementation of the CW flux observer an arduous process. The PW and CW currents can be easily measured through current sensors, whereas the RW current is not directly accessible. Moreover, when the PW is connected to the ideal grid, the PW flux will keep constant. Therefore, as for control feasibility, PW current $\boldsymbol{i}_{ps}$, CW current $\boldsymbol{i}_{cs}$, and PW flux $\boldsymbol{\psi}_{ps}$ are chosen as state variables. The state space equation of the BDFTSIG can be derived from voltage equations (5)–(7) and current expression (8) as

$$s\boldsymbol{X} = \boldsymbol{A}\boldsymbol{X} + \boldsymbol{B}\boldsymbol{V} \tag{9}$$

where $\boldsymbol{X} = [\boldsymbol{i}_{ps}^{g}\ (\boldsymbol{i}_{cs}^{g} e^{j\theta h})^*\ \boldsymbol{\psi}_{ps}^{g}]^T$ are state variables, $\boldsymbol{V} = [\boldsymbol{v}_{ps}^{g}\ (\boldsymbol{v}_{cs}^{g} e^{j\theta h})^*\ \boldsymbol{0}]^T$ are the stator and rotor voltage vectors,

$$\boldsymbol{A} = \begin{bmatrix} A_{11} & A_{12} & A_{13} \\ A_{21} & A_{22} & A_{23} \\ A_{31} & A_{32} & A_{33} \end{bmatrix}, \boldsymbol{B} = \begin{bmatrix} B_{11} & B_{12} & B_{13} \\ B_{21} & B_{22} & B_{23} \\ B_{31} & B_{32} & B_{33} \end{bmatrix}$$

and the expressions of matrix elements in $\boldsymbol{A}$ and $\boldsymbol{B}$ are defined in the Appendix A.

By using Euler discretization, the state space equation represented by (9) is transformed to discrete-time domain as

$$\boldsymbol{X}(k+1) = \boldsymbol{X}(k) + T_s\left(\boldsymbol{A}\boldsymbol{X}(k) + \boldsymbol{B}\boldsymbol{V}(k)\right) \tag{10}$$

where $k \in N$ denotes the time step, and T_s is the sampling interval.

B. Predictive Power Model

The complex power of PW can be calculated as

$$\boldsymbol{S_p} = P_p + jQ_p = \frac{3}{2}\boldsymbol{i}_{ps}^{g*}\boldsymbol{v}_{ps}^{g}. \tag{11}$$

By differentiating the complex power in (11) with respect to time t, the complex power variation can be obtained as

$$\frac{d\boldsymbol{S_p}}{dt} = \frac{3}{2}\left(\frac{d\boldsymbol{i}_{ps}^{g\ *}}{dt}\boldsymbol{v}_{ps}^{g} + \boldsymbol{i}_{ps}^{g*}\frac{d\boldsymbol{v}_{ps}^{g}}{dt}\right). \tag{12}$$

When the PW is connected to the utility grid which provides sinusoidal and balanced supply, the PW voltage and its relation to PW flux can be expressed as

$$\boldsymbol{v}_{ps}^{g} = \left|\boldsymbol{v}_{ps}^{g}\right| e^{j(\omega_p - \omega_g)t} \tag{13}$$

$$\boldsymbol{\psi}_{ps}^{g} = \frac{\boldsymbol{v}_{ps}^{g}}{j\omega_p}. \tag{14}$$

Substituting the first equation of (8) and (9) into (12), and considering (11), (13), and (14), the complex power variation in continuous time can be expressed as

$$\frac{d\boldsymbol{S}_p}{dt} = \Lambda_1\boldsymbol{S}_p + \Lambda_2\left(\boldsymbol{i}_{cs}^{g}e^{j\theta_h}\right)\boldsymbol{v}_{ps}^{g} + \Lambda_3\left(\boldsymbol{v}_{cs}^{g}e^{j\theta_h}\right)\boldsymbol{v}_{ps}^{g} + \Lambda_4\left|\boldsymbol{v}_{ps}^{g}\right|^2 \tag{15}$$

with the expressions of coefficients $\Lambda_1 \sim \Lambda_4$ being defined in the Appendix B. As the mechanical speed ω_m is assumed to be constant within one prediction horizon, it can be considered as a model parameter rather than a state variable [32].

The controller to be developed in this paper operates in discrete time with fixed sampling period. By using Euler discretization, the continuous-time model of complex power represented

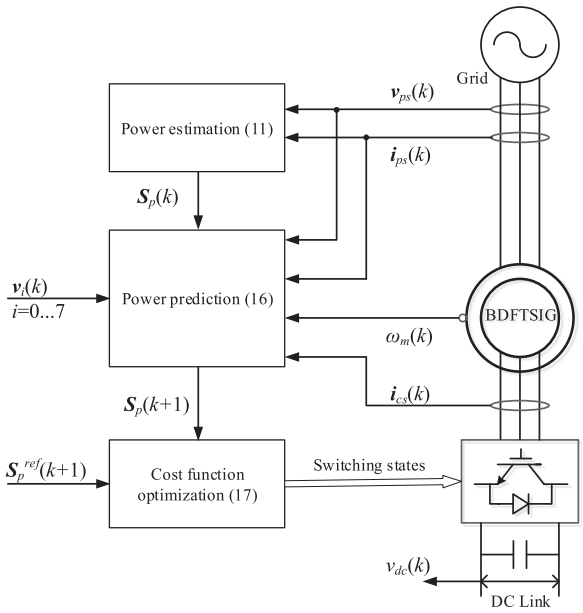

Fig. 4. Control structure of the FS-MPPC controller for the BDFTSIG.

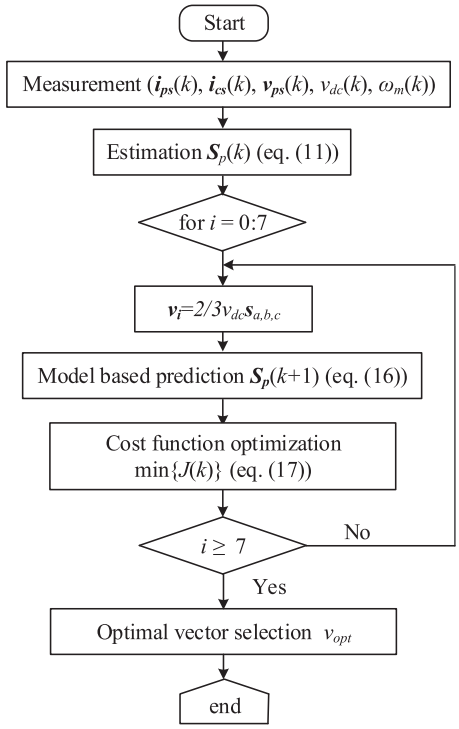

Fig. 5. Flowchart of the FS-MPPC controller for the BDFTSIG.

by (15) is transformed to discrete-time domain as

$$\boldsymbol{S}_p(k+1) = \boldsymbol{S}_p(k) + T_s \begin{pmatrix} \Lambda_1 \boldsymbol{S}_p(k) + \Lambda_2 \left(\boldsymbol{i}_{cs}^g(k) e^{j\theta_h}\right) \boldsymbol{v}_{ps}^g(k) \\ +\Lambda_3 \left(\boldsymbol{v}_{cs}^g(k) e^{j\theta_h}\right) \boldsymbol{v}_{ps}^g(k) + \Lambda_4 \left|\boldsymbol{v}_{ps}^g(k)\right|^2 \end{pmatrix}. \quad (16)$$

Equation (16) indicates that $\boldsymbol{S}_p(k+1)$, the complex power at time instant $k+1$, can be predicted by PW current, CW current, PW voltage, and CW voltage at time instant k, being denoted with $\boldsymbol{i}_{ps}(k)$, $\boldsymbol{i}_{cs}(k)$, $\boldsymbol{v}_{ps}(k)$ and $\boldsymbol{v}_{cs}(k)$, respectively.

IV. FS-MPPC Controller Development

The schematic diagram of the FS-MPPC controller for the BDFTSIG in grid connected operation is illustrated in Fig. 4. The control law is defined as minimizing power error and limiting the maximum current, which can be translated into the cost function with following structure

$$J(k) = \left|P_p{}^{\mathrm{ref}} - P_p(k+1)\right| + \left|Q_p{}^{\mathrm{ref}} - Q_p(k+1)\right| + I_m(k+1) \quad (17)$$

$$I_m(k+1) = \begin{cases} \gamma >> 0, & \text{if } \left|\boldsymbol{i}_{ps}^g(k+1)\right| > \left|\boldsymbol{i}_{\max}\right| \\ 0, & \text{if } \left|\boldsymbol{i}_{ps}^g(k+1)\right| \leq \left|\boldsymbol{i}_{\max}\right| \end{cases} \quad (18)$$

where P_p^{ref} and Q_p^{ref} are the reference values of the active power and reactive power. $P_p(k+1)$ and $Q_p(k+1)$ are obtained by decomposing the complex power $\boldsymbol{S}_p(k+1)$ into real and imaginary parts. $\boldsymbol{i}_{ps}^g(k+1)$ is the predicted PW current which can be obtained by the first equation in (10). $\boldsymbol{i}_{\max}$ is the maximum stator current, when the absolute value of the predicted current is higher than the limitation value, the term I_m will step to a very high value, otherwise, I_m will remain at zero. In this study, the weighting factor is chosen as 1 in which case the controller allocates equal control weight to active power and reactive power. Only horizon-one prediction is considered in order not to increase the computational burden.

The realization of the developed FS-MPPC controller is to find the optimal voltage vector that minimizes the defined cost function in (17), and then apply it to achieve the desired performance at the next sampling instant. The overall flowchart of the execution process for the developed FS-MPPC controller is shown in Fig. 5, detailed in the following steps.

Step 1) *Measurement:* The PW current $\boldsymbol{i}_{ps}(k)$, PW voltage $\boldsymbol{v}_{ps}(k)$, CW current $\boldsymbol{i}_{cs}(k)$, dc-bus voltage $v_{\mathrm{dc}}(k)$, and rotational speed of BDFTSIG $\omega_m(k)$ at kth instant are measured.

Step 2) *Power estimation:* The complex power of PW $\boldsymbol{S}_p(k)$ is estimated by the measured $\boldsymbol{i}_{ps}(k)$ and $\boldsymbol{v}_{ps}(k)$ according to (11).

Step 3) *Voltage vector construction:* CW voltage $\boldsymbol{v}_{cs}$ is equal to the inverter output voltage $\boldsymbol{v}_i$. For a two-level voltage source inverter, $\boldsymbol{v}_i$ can be constructed by dc-bus voltage v_{dc} and the switching states $\boldsymbol{s}_{a,b,c}$ as $\boldsymbol{v}_i = 2/3 v_{dc} \boldsymbol{s}_{a,b,c}, i = 0 \ldots 7$.

Step 4) *Power prediction:* Based on the measurement and power estimation, the complex power of PW $\boldsymbol{S}_p(k+1)$ at instant $k+1$ can be predicted by the model expressed in (16).

Step 5) *Cost function optimization:* The cost function optimization principle is defined as the minimization of future power error and the limitation of the maximum current during each sampling period.

Step 6) *Voltage vector selection:* The voltage vector that minimizes the cost function is selected as the optimal vector v_{opt} to be applied. Return to step 1).

TABLE II
KEY PARAMETERS

Parameters	Value	Value
Rated power P_N	1 kW	20 kW
Rated voltage v_N	190 V	415 V
Pole pair number $p_{p(c)}$	3	2
Stator resistance $R_{ps(cs)}$	4.6 Ω	0.207 Ω
Rotor resistance $R_{pr(cr)}$	5.5 Ω	0.218 Ω
Magnetizing inductance $L_{pM(cM)}$	210 mH	85 mH
Stator leakage inductance $L_{ps\sigma(cs\sigma)}$	9 mH	2.4 mH
Rotor leakage inductance $L_{pr\sigma(cr\sigma)}$	18 mH	2.4 mH
DC bus voltage v_{dc}	250 V	400 V
Converter operation frequency f_c	–10 Hz~10 Hz	–10 Hz~10 Hz
Sampling period T_s	100 μs	100 μs

The mathematic expression of the developed FS-MPPC controller can be summarized as

$$\begin{cases} \boldsymbol{S}_p(k+1) = \boldsymbol{S}_p(k) \\ \quad +T_s \begin{pmatrix} \Lambda_1 \boldsymbol{S}_p(k) + \Lambda_2 \left(\boldsymbol{i}_{cs}^g(k) e^{j\theta_h}\right) \boldsymbol{v}_{ps}^g(k) \\ +\Lambda_3 \left(\boldsymbol{v}_i^g(k) e^{j\theta_h}\right) \boldsymbol{v}_{ps}^g(k) + \Lambda_4 \left|\boldsymbol{v}_{ps}^g(k)\right|^2 \end{pmatrix} \\ J(k) = \left|{P_p}^{\text{ref}} - P_p(k+1)\right| + \left|{Q_p}^{\text{ref}} - Q_p(k+1)\right| \\ \quad +I_m(k+1) \\ \boldsymbol{v_i} : \min\{J(k)\} \\ \qquad\qquad i = 0, 1, \ldots, 7. \end{cases} \tag{19}$$

As the power relationship is independent of specific frame, the predictive power model has the same form and characteristics in different reference frames. The developed FS-MPPC controller is not restricted to a specific reference frame, and the only thing to be noted is that all the variables should be expressed in the same frame.

The mathematic expression in (19) reveals that the developed FS-MPPC controller only needs the information of variables which are easy to be measured, and the CW flux observer that is applied in DPC/DTC controllers is no longer required. Unlike the existing controllers for BDFIMs in which the influence of rotor circuit is omitted by neglecting the rotor resistance, no attempts of simplification and linearization in the electrical model are carried out in the developed FS-MPPC controller. The influence of rotor circuit is embedded within the predictive power model and being inherently considered.

V. NUMERICAL SIMULATION VERIFICATION

Before the experimental verification, closed-loop simulations are performed in MATLAB to benchmark the performance of the developed FS-MPPC controller for the BDFTSIG system. Table II lists the key parameters of BDFTSIG systems rated at 1 kW and 20 kW, respectively.

A. Performance Under Various Reference Frames

Fig. 6 shows the simulation results of the developed FS-MPPC controller under various reference frames, which are specifically listed in Table I. The parameters of 1 kW BDFTSIG system are adopted, and the results of active power and reactive power are given. It can be observed from Fig. 6 that the developed FS-MPPC controller has almost the same performance when the control algorithm is executed in different reference frames. This demonstrate that, unlike conventional VC controller in which an appropriate reference frame has to be determined first, the developed FS-MPPC controller is not restricted to a specific reference frame.

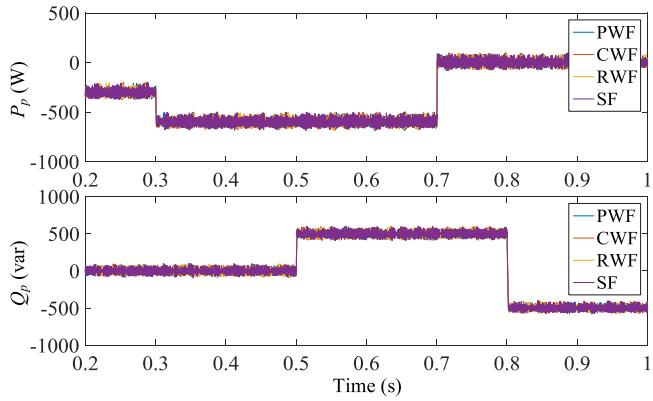

Fig. 6. Responses of active power and reactive power under various reference frames.

B. Performance Under Different Power Levels

Fig. 7 shows the simulation results of the developed FS-MPPC controller for BDFTSIG systems with different rated power. The results of active power, reactive power, and switching frequency for the 20 kW system are given in Fig. 7(a), and the corresponding results of the 1 kW system are given in Fig. 7(b). The switching frequency is calculated every 0.05 s under steady-state operation. It is obviously observed that the developed FS-MPPC controller can achieve similar performance for BDFTSIG systems rated at 1 kW and 20 kW, respectively. Unlike the conventional vector control, there is no need to tuning parameters regarding different power levels. It should be noted that the developed FS-MPPC controller has low switching frequency, with the average value situated around 1.25 kHz, which shows apparent advantage for high power systems.

C. Performance Comparison With VC Controller

To validate the superiority of the developed FS-MPPC controller, it is compared with an improved and well-tuned vector controller in [33]. The improved vector controller incorporating appropriate feedforward items has been demonstrated to have better dynamic performance than the conventional vector controllers for BDFIMs. The parameters of the 1 kW BDFTSIG system are adopted, and the two control algorithms are compared under the same condition. As been presented in Fig. 7, the average switching frequency of the developed FS-MPPC controller is around 1.25 kHz. Therefore, the switching frequency of the improved vector controller is set at 1.25 kHz to ensure equal condition in comparison. The results of active power, reactive power, voltage, and current under ideal grid condition

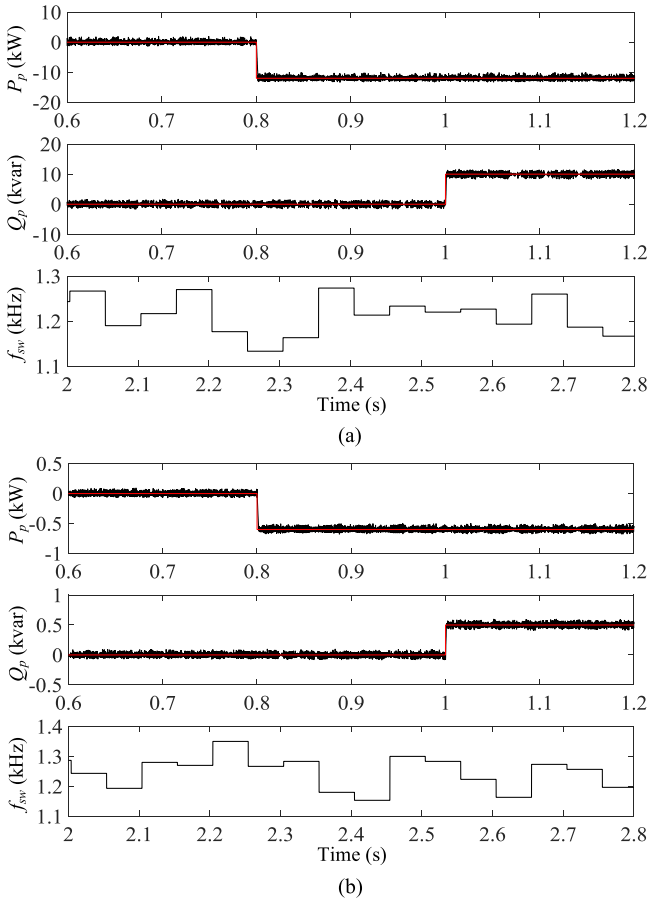

Fig. 7. Responses of active power, reactive power and switching frequency. (a) 20 kW BDFTSIG system. (b) 1 kW BDFTSIG system.

are given in Fig. 8. It is demonstrated that the developed FS-MPPC controller can achieve considerably faster response than the improved vector controller.

D. Performance Under Grid Fault Condition

Fig. 9 gives the responses of the developed FS-MPPC controller under grid fault condition. The grid voltage symmetrically droops to 20% of the rated value at 1.2 s. In order to relieve the transient effect, the dc-bus voltage is set at a higher value (350 V). When the grid fault is detected, the reference value of active power is set at 0 W, and the reference value of reactive power is set according to the maximum value of PW current ($\boldsymbol{i}_{\max} = 4\,A, Q_p^{ref} = 3\boldsymbol{v}_{ps}\boldsymbol{i}_{\max}$). It can be observed that effective control of active power and reactive power is maintained during grid fault and the current is effectively restricted by the limitation term defined in the cost function presented in (17).

Apart from the symmetrical grid fault, asymmetrical grid fault is also an important issue for grid connected operation of the BDFTSIG. For the developed FS-MPPC controller in this paper, it is feasible to achieve good performance under asymmetrical grid fault condition by incorporating the power compensation strategies proposed in [17], [26], [34], and [35] without modifying the control structure in Fig. 4. However, thorough discussion

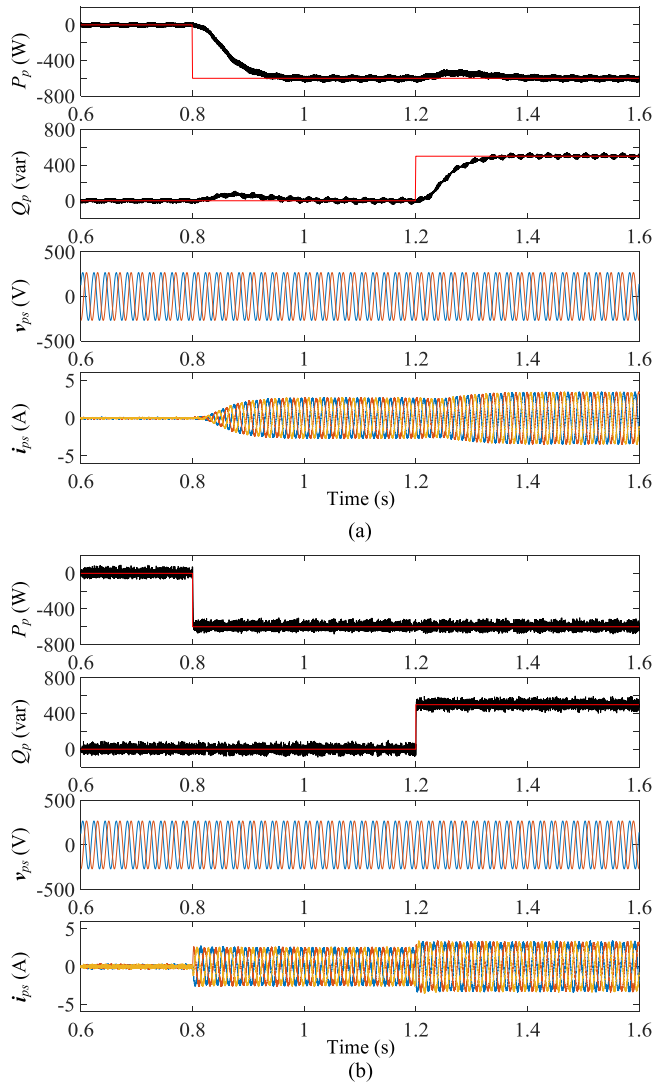

Fig. 8. Responses under ideal grid condition. (a) Improved VC controller. (b) Developed FS-MPPC controller.

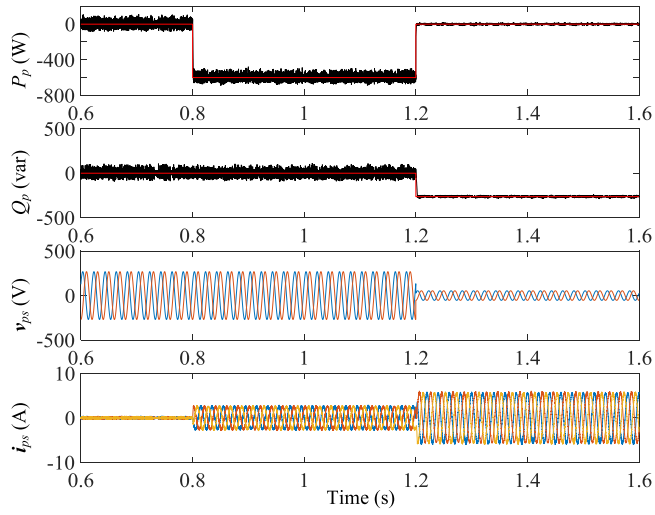

Fig. 9. Responses of the FS-MPPC controller under grid fault condition.

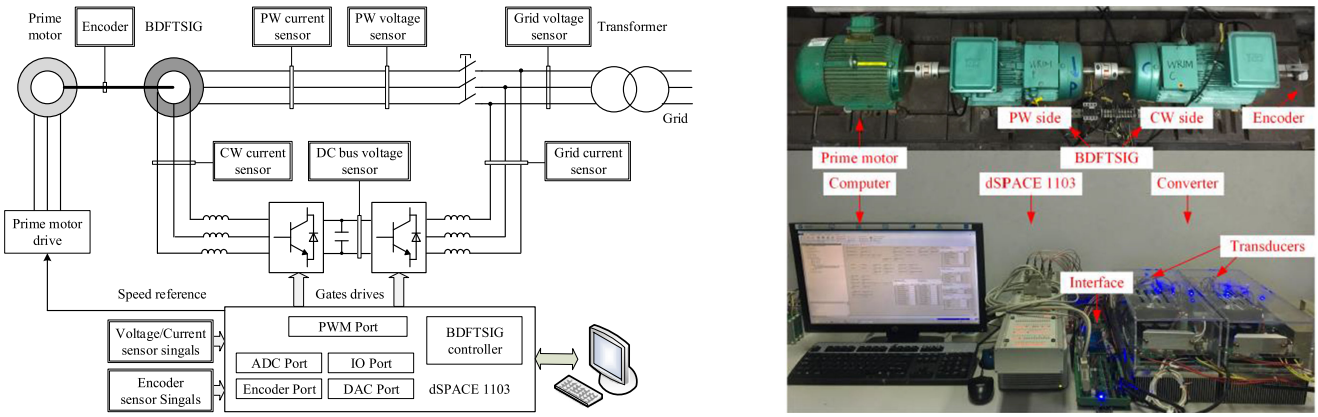

Fig. 10. Framework of the BDFTSIG system. (a) System diagram. (b) Photograph.

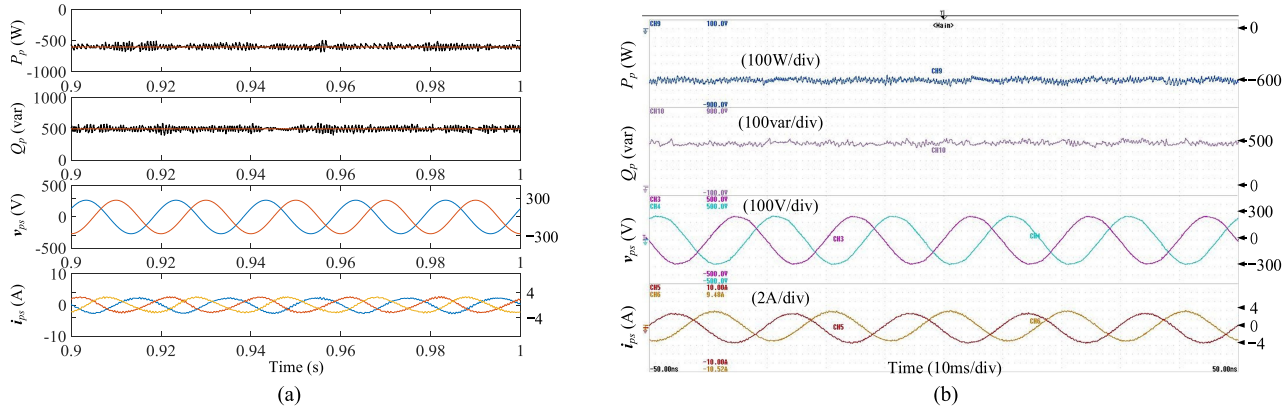

Fig. 11. Simulation and experimental results under steady-state operation ($n = 400\,\mathrm{r/min}, P_p = -600\,\mathrm{W}, Q_p = 500\,\mathrm{var}$). (a) Simulation results. (b) Experimental results.

on operation under asymmetrical grid fault condition is out of scope of this paper and is not further expanded.

VI. Experimental Test Verification

To further validate the effectiveness of the developed FS-MPPC controller, experimental tests are carried out on an experimental BDFTSIG system. Fig. 10(a) and (b) shows the block diagram and photograph of the experimental BDFTSIG system. The prototype BDFTSIG is formulated by cascading two identical WRIMs on a common shaft. The rotor windings of the two WRIMs are interconnected so as to produce contra rotating magnetic fields for effective synchronous operation [10], [29], [30]. PW of the BDFTSIG is connected to the three-phase grid via a variac and CW of the BDFTSIG via a power converter. The BDFTSIG is rated at 1 kW, with an operation range of 400–600 r/min (±20% of natural synchronous speed). Key parameters of the BDFTSIG are listed in Table II. As the BDFTSIG has small magnetizing inductance and large leakage inductance, if the grid voltage (380 V) is applied to the PW side, most of the CW current is used for excitation and fails to output enough active current. Therefore, the rated voltage is scaled down to 190 V for possible power control. The PW current and voltage, the CW current, and the dc-bus voltage are measured directly through voltage transducers (LV25-p) and current transducers (LA25-p). The CW voltage is constructed by switching states of the converter and the measured dc-bus voltage. The BDFTSIG is mechanically coupled to a prime motor driven in speed mode. A two-level IGBT converter is driven by the dSPACE 1103 controller board to control the voltage and frequency supplied to the CW of BDFTSIG. The dc-bus voltage is maintained at 250 V by the converter. By considering both the steady-state performance and the computational capacity of the processor, the sampling period of the developed FS-MPPC controller is set at 100 μs.

Figs. 11–16 illustrate simulation and experimental results considering different operation situations. Only two line-voltages of PW are directly measured through voltage transducer, through which the three phase-voltages can then be directly calculated. In the simulations, the three phase-currents of PW are measured. Whereas in the experiments, only two phase-currents of PW are measured, and the third phase-current can be easily calculated through the measured currents.

Fig. 11 illustrates the simulation and experimental results under steady-state operation. From top to bottom, the curves are active power, reactive power, line-voltage of PW, and phase

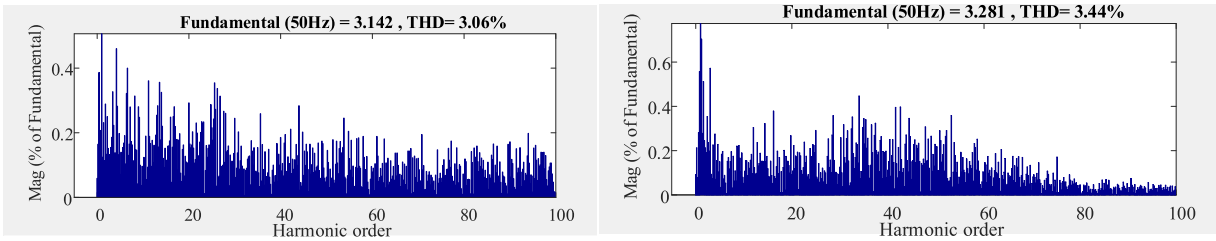

(a) (b)

Fig. 12. Harmonic spectrum of PW current under steady-state operation ($n = 400\,\mathrm{r/min}, P_p = -600\,\mathrm{W}, Q_p = 500\,\mathrm{var}$). (a) Simulation results. (b) Experimental results.

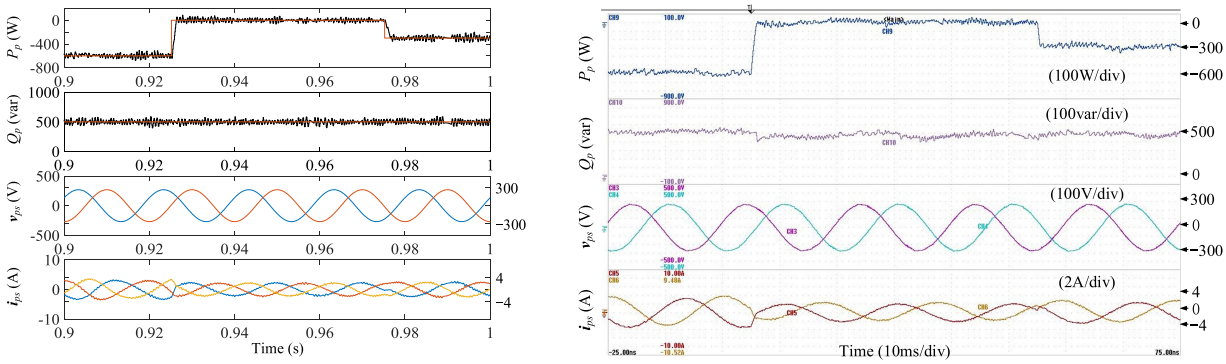

(a) (b)

Fig. 13. Simulation and experimental results under the condition of stepped changes in active power reference ($n = 400$ r/min; P_p steps from -600 W to 0 W, and then steps to -300 W; $Q_p = 500$ var). (a) Simulation results. (b) Experimental results.

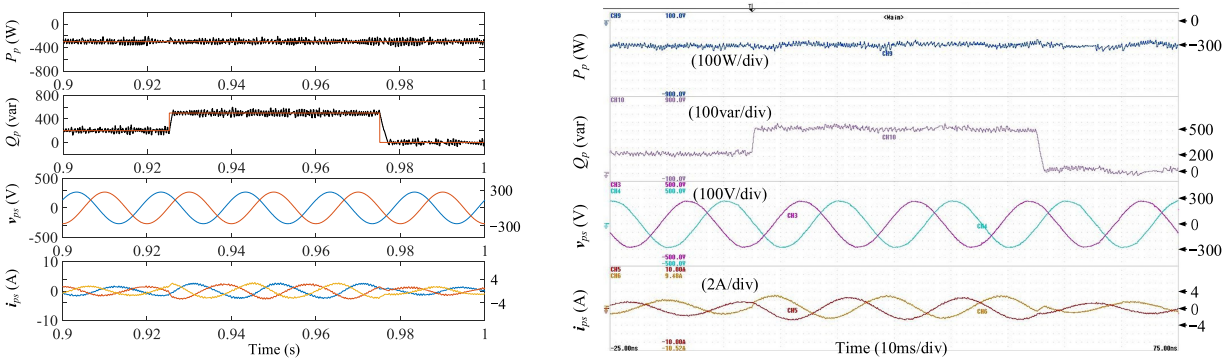

(a) (b)

Fig. 14. Simulation and experimental results under the condition of stepped changes in reactive power reference ($n = 400$ r/min; $P_p = -300$ W; Q_p steps from 200 var to 500 var, and then steps to 0 var). (a) Simulation results. (b) Experimental results.

current of PW. The BDFTSIG operates at subsynchronous speed 400 r/min, the commending value of active power is –600 W, and the commending value of reactive power is 500 var. The experimental results match the simulation results quite well, showing that the developed FS-MPPC controller can achieve accurate power control with good steady-state performance. The results of harmonic spectrum for PW current $\boldsymbol{i}_{ps}$ under steady-state are presented in Fig. 12. It can be observed that the simulation and experimental waveforms have similar harmonic spectrum, with THD value in experiment (3.44%) slightly higher than that in simulation (3.06%).

Figs. 13 and 14 present the simulation and experimental results under the condition of stepped changes in active power reference and reactive power reference, respectively, with the BDFTSIG operating at a constant rotor speed 400 r/min. Both active power and reactive power can settle down to the commanding values within 2 ms. When the active power steps the reactive power remains unchanged, and vice versa, demonstrating excellent decoupled control between active power and reactive power. It can also be observed that the frequency of PW current is maintained at 50 Hz, and its amplitude changes according to the values of active power and reactive power. In Figs. 13 and 14,

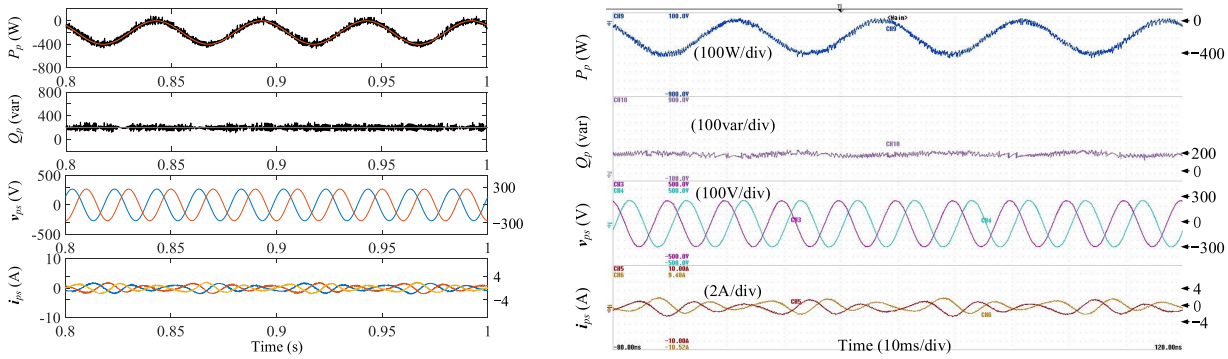

(a) (b)

Fig. 15. Simulation and experimental results under the condition of various active power reference ($n = 400$ r/min; $Q_p = 200$ var; P_p is generated by a 20 Hz sinusoidal waveform with a peak-to-peak value of 400 W). (a) Simulation results. (b) Experimental results.

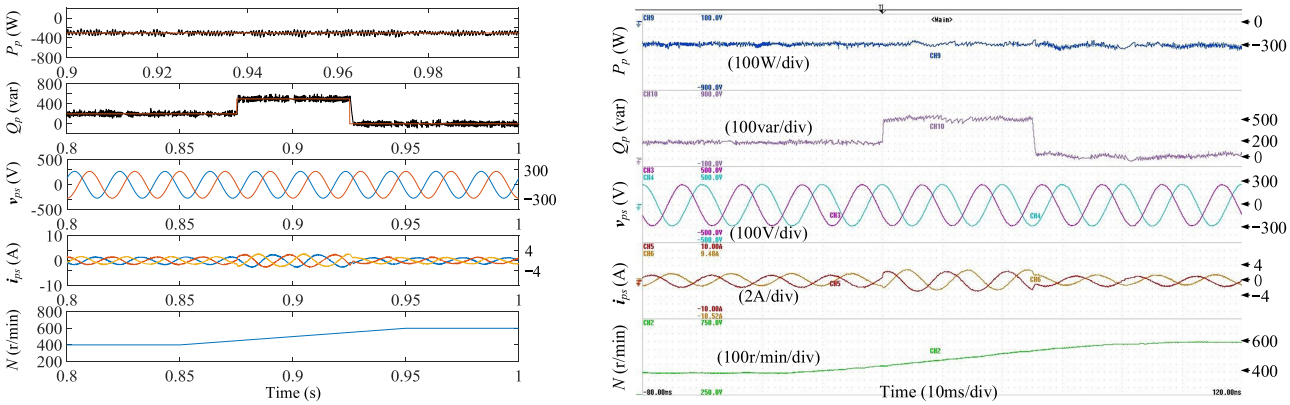

(a) (b)

Fig. 16. Simulation and experimental results under the condition of various speed (n varies from 400 r/min to 600 r/min; $P_p = -300$ W; Q_p steps from 200 var to 500 var, and then steps to 0 var). (a) Simulation results. (b) Experimental results.

the experimental results agree well with those from simulations, demonstrating excellent transient-state performance of the developed FS-MPPC controller.

To further evaluate the tracking performance of the developed FS-MPPC controller, Fig. 15 depicts the simulation and experimental results obtained under various active power. The active power reference is generated by a 20 Hz sinusoidal waveform with a peak-to-peak value of 400 W. The commending value of reactive power is 200 var. As can be obviously observed, the active power can track the varying commending values very well without affecting the performance of reactive power, and the experimental results match the simulation results quite well.

Moreover, the condition when operation speed varies from subsynchronous 400 r/min to super-synchronous 600 r/min is tested. The simulation and experimental results are presented in Fig. 16. As can be noted, the agreement between the experiment and simulation is quite satisfactory. During speed variation, the reactive power steps according to its commanding value from 200 var to 500 var, and then steps to 0 var, achieving both good steady-state and transient-state performance. The active power is successfully maintained at -300 W, demonstrating excellent decoupled control between active power and reactive power. It can also be observed that when the speed is varying, the frequency of PW current is maintained at 50 Hz, demonstrating the VSCF operation.

VII. Conclusion

In this paper, FS-MPPC controller for the BDFTSIG has been theoretically developed and experimentally implemented for the first time, achieving accurate and decoupled power control with excellent steady-state and transient-state performance.

1) The dynamic model of the BDFTSIG is described in the general reference frame from which all other reference frames can be deduced readily.
2) A predictive power model, which clearly reveals the relationship between the input voltage vector and the future power behavior, is derived in the general reference frame. The developed FS-MPPC controller is not restricted to a specific reference frame, and this reference frame-free feature contributes to high flexibility and universality.
3) The CW flux observer is no longer required in the developed FS-MPPC controller, which significantly decreases the complexity of the control system. The active/reactive

power at the next sample instant is predicted by the developed power model that is based on the easily obtained variables, and the control objectives of power error minimization and maximum current limitation are mapped into the cost function. The realization of the developed FS-MPPC controller is to find the optimal voltage vector that optimizes the defined cost function, and then apply the selected vector to achieve the control objectives.

4) The developed FS-MPPC controller makes no attempts of simplification and linearization in the electrical model. The influence of rotor circuit is embedded within the predictive power model and being inherently considered, which contributes to accurate power control of the BDFTSIG.
5) Numerical simulations considering various reference frames and different power levels are performed, which reveals that the developed FS-MPPC controller can achieve the same good performance without changing structure or parameters of the controller. Besides, the feasibility and effectiveness of the developed FS-MPPC controller under grid fault conditions are validated and briefly discussed.
6) Experimental tests are carried out on a prototype BDFTSIG system, with the results demonstrating the effectiveness of the developed FS-MPPC controller.

APPENDIX A

The elements of matrixes $\boldsymbol{A}$ and $\boldsymbol{B}$ in (9) are defined as follows:

$$A_{11} = -\lambda(L_{cs}L_r - L_{cM}^2)R_{ps} - \lambda L_{cs}L_{ps}R_r - j(\omega_g - p_p\omega_m) - jp_c\omega_m\lambda L_{cM}^2 L_{ps}$$

$$A_{12} = \lambda L_{pM}L_{cM}R_{cs} - jp_c\omega_m\lambda L_{pM}L_{cM}L_{cs}$$

$$A_{13} = \lambda L_{cs}R_r - jp_p\omega_m\lambda L_{cs}L_r + j(p_p + p_c)\omega_m\lambda L_{cM}^2$$

$$A_{21} = \lambda L_{pM}L_{cM}R_{ps} + \lambda L_{ps}^2\frac{L_{cM}}{L_{pM}}R_r + jp_c\omega_m\lambda L_{ps}(L_{ps}L_r - L_{pM}^2)\frac{L_{cM}}{L_{pM}}$$

$$A_{22} = -\lambda(L_{ps}L_r - L_{pM}^2)R_{cs} - j(\omega_g - p_p\omega_m) + jp_c\omega_m\lambda(L_{ps}L_r - L_{pM}^2)L_{cs}$$

$$A_{23} = -\lambda L_{ps}\frac{L_{cM}}{L_{pM}}R_r + jp_p\omega_m L_{pM}L_{cM} - jp_c\omega_m\lambda(L_{ps}L_r - L_{pM}^2)\frac{L_{cM}}{L_{pM}}$$

$$A_{31} = -R_{ps}, A_{32} = 0, A_{33} = -j\omega_g$$

$$B_{11} = \lambda(L_{cs}L_r - L_{cM}^2), B_{12} = -\lambda L_{pM}L_{cM}, B_{13} = 0$$

$$B_{21} = -\lambda L_{pM}L_{cM}, B_{22} = \lambda(L_{ps}L_r - L_{pM}^2), B_{23} = 0$$

$$B_{31} = 1, B_{32} = 0, B_{33} = 0.$$

APPENDIX B

The coefficients in (15) are shown as follows:

$$\Lambda_1 = -\lambda L_{ps}L_{cs}R_r + j\omega_1 - jp_p\omega_m\lambda L_{cs}(L_{ps}L_r - L_{pM}^2) - \lambda(L_{cs}L_r - L_{cM}^2)R_{ps} + j(p_p + p_c)\omega_m\lambda L_{ps}L_{cM}^2$$

$$\Lambda_2 = \frac{3}{2}\lambda L_{pM}L_{cM}(R_{cs} + jp_c\omega_m L_{cs}), \Lambda_3 = -\frac{3}{2}\lambda L_{pM}L_{cM}$$

$$\Lambda_4 = \frac{3}{2}\lambda((jL_{cs}R_r - p_p\omega_m L_{cs}L_r + (p_p + p_c)\omega_m L_{cM}^2)\frac{1}{\omega_p} + (L_{cs}L_r - L_{cM}^2)).$$

REFERENCES

[1] M. Cheng, P. Han, G. Buja, and G. M. Jovanović, "Emerging multiport electrical machines and systems: Past developments, current challenges and future prospects," *IEEE Trans. Ind. Electron.*, vol. 65, no. 7, pp. 5422–5435, Jul. 2018.

[2] M. Cheng and Y. Zhu, "The state of the art of wind energy conversion systems and technologies: A review," *Energy Convers. Manage.*, vol. 88, pp. 332–347, Dec. 2014.

[3] D. G. Dorrell and M. Jovanoviü, "On the possibilities of using a brushless doubly-fed reluctance generator in a 2 MW wind turbine," in *Proc. IEEE Ind. Appl. Soc. Annu. Meeting*, Oct. 2008, pp. 1–8.

[4] L. Xu, B. Guan, H. Liu, L. Gao, and K. Tsai, "Design and control of a high-efficiency doubly-fed brushless machine for wind power generator application," in *Proc. IEEE Energy Convers. Congr. Expo.*, Sep. 2010, pp. 2409–2416.

[5] X. Chen, Z. Wei, X. Gao, C. Ye, and X. Wang, "Research of voltage amplitude fluctuation and compensation for wound rotor brushless doubly-fed machine," *IEEE Trans. Energy Convers.*, vol. 30, no. 3, pp. 908–917, Sep. 2015.

[6] I. A. Gowaid, A. S. Abdel-khalik, A. M. Massoud, and S. Ahmed, "Ride-through capability of grid-connected brushless cascade DFIG wind turbines in faulty grid conditions: A comparative study," *IEEE Trans. Sustain. Energy*, vol. 4, no. 4, pp. 1002–1015, Oct. 2013.

[7] R. Li, A. K.Wallace, and R. Spee, "Determination of converter control algorithms for brushless doubly-fed induction motor drives using Floquet and Lyapunov techniques," *IEEE Trans. Power Electron.*, vol. 10, no. 1, pp. 78–85. Jan. 1995.

[8] C. Brune, R. Spee, and A. K. Wallace, "Experimental evaluation of a variable- speed, doubly-fed wind-power generation system," *IEEE Trans. Ind. Appl.*, vol. 30, no. 3, pp. 648–655, Jun. 1994.

[9] B. Hopfensperger, D. J. Atkinson, and R. A. Lakin, "Stator flux oriented control of a cascaded doubly-fed induction machine," *IEE Proc. Elect. Power Appl.*, vol. 146, no. 6, pp. 597–605, Nov. 1999.

[10] D. Basic, J. G. Zhu, and G. Boardman, "Transient performance study of a brushless doubly fed twin stator induction generator," *IEEE Trans. Energy Convers.*, vol. 18, no. 3, pp. 400–408, Sep. 2003.

[11] S. Shao, E. Abdi, F. Barati, and R. McMahon, "Stator-flux-oriented vector control for brushless doubly fed induction generator," *IEEE Trans. Ind. Electron.*, vol. 56, no. 10, pp. 4220–4228, Oct. 2009.

[12] G. Zhang *et al.*, "A robust control Scheme based on ISMC for the brushless doubly fed induction machine," *IEEE Trans. Power Electron.*, vol. 33, no. 4, pp. 3129–3140, Apr. 2018.

[13] X. Wei, M. Cheng, W. Wang, P. Han, and R. Luo, "Direct voltage control of dual-stator brushless doubly-fed induction generator for stand-alone wind energy conversion systems," *IEEE Trans. Magn.*, vol. 25, no. 7, Jul. 2016, Art. no. 8203804.

[14] L. Sun *et al.*, "Decoupling network design for inner current loops of stand-alone brushless doubly fed induction generation power system," *IEEE Trans. Power Electron.*, vol. 33, no. 2, pp. 957–963. Feb. 2018.

[15] J. Chen, W. Zhang, B. Chen, and Y. Ma, "Improved vector control of brushless doubly fed induction generator under unbalanced grid conditions for offshore wind power generation," *IEEE Trans. Energy Convers.*, vol. 31, no. 2, pp. 293–302, Jan. 2016.

[16] I. Sarasola, J. Poza, M. A. Rodriguez, and G. Abad, "Direct torque control design and experimental evaluation for the brushless doubly fed machine," *Energy Convers. Manage.*, vol. 52, no. 2, pp. 1226–1234, Feb. 2011.

[17] J. Hu, J. Zhu, and D. G. Dorrell, "A new control method of cascaded brushless doubly fed induction generators using direct power control," *IEEE Trans. Energy Convers.*, vol. 29, no. 3, pp. 771–779, Sep. 2014.
[18] F. Zhang *et al.*, "Controller strategy for open-winding brushless doubly-fed wind power generator with common mode voltage elimination," *IEEE Trans. Ind. Electron.*, to be published. doi: 10.1109/TIE.2018.2811370.
[19] J. Hang, J. Zhang, M. Cheng, and J. Huang, "Online interturn fault diagnosis of permanent magnet synchronous machine using zero-sequence components," *IEEE Trans. Power Electron.*, vol. 30, no. 12, pp. 6731–6741, Dec. 2015.
[20] R. Sadeghi, S. M. Madani, and M. Ataei, "A new smooth synchronization of brushless doubly-fed induction generator by applying a proposed machine model," *IEEE Trans. Sustain. Energy*, vol. 9, no. 1, pp. 371–380, Jan. 2018.
[21] X. Wei, M. Cheng, P. Han, W. Wang, and R. Luo, "Comparison of control strategies for a novel dual-stator brushless doubly-fed induction generator in wind energy applications," in *Proc. IEEE Int. Conf. Elect. Mach. Syst.*, Oct. 2015, pp. 1039–1045.
[22] M. Cheng, F. Yu, K. T. Chau, and W. Hua, "Dynamic performance evaluation of a nine-phase flux-switching permanent-magnet motor drive with model predictive control," *IEEE Trans. Ind. Electron.*, vol. 63, no. 7, pp. 4539–4549, Jul. 2016.
[23] Y. Zhang and H. Yang, "Generalized two-vector-based model-predictive torque control of induction motor drives," *IEEE Trans. Power Electron.*, vol. 30, no. 7, pp. 3818–3829, Jul. 2015.
[24] H. Yang *et al.*, "Sliding-mode observer based voltage-sensorless model predictive power control of PWM rectifier under unbalanced grid condition," *IEEE Trans. Ind. Electron.*, vol. 65, no. 7, pp. 5550–5560, Jul. 2018.
[25] X. Wang and D. Sun, "Three-vector-based low-complexity model predictive direct power control strategy for doubly fed induction generators," *IEEE Trans. Power Electron.*, vol. 32, no. 1, pp. 773–782, Jan. 2017.
[26] D. Sun and X. Wang, "Low-complexity model predictive direct power control for DFIG under both balanced and unbalanced grid conditions," *IEEE Trans. Ind. Electron.*, vol. 63, no. 8, pp. 5186–5196, Aug. 2016.
[27] R. Aguilera *et al.*, "Selective harmonic elimination model predictive control for multilevel power converters," *IEEE Trans. Power Electron.*, vol. 32, no. 3, pp. 2416–2426, Mar. 2017.
[28] R. P. Aguilera and D. E. Quevedo, "Predictive control of power converters: Designs with guaranteed performance," *IEEE Trans. Ind. Informat.*, vol. 11, no. 1, pp. 53–63, Feb. 2015.
[29] N. Chilakapati, V. S. Ramsden, and V. Ramaswamy, "Performance evaluation of doubly-fed twin stator induction machine drive with voltage and current space vector control schemes," *IEE Proc. Elect. Power Appl.*, vol. 148, no. 3, pp. 287–292, May 2001.
[30] G. Boardman, J. G. Zhu, and Q. P. Ha, "General reference frame modelling of the doubly fed induction machine using space vectors," in *Proc. Australasian Power Eng. Conf.*, Sep. 2002, pp. 1–6.
[31] X. Wei, M. Cheng, J. Zhu, H. Yang, and W. Hua, "Model predictive power control of a brushless doubly fed twin stator induction generator," in *Proc. IEEE Energy Convers. Congr. Expo.*, Oct. 2017, pp. 5080–5085.
[32] T. Geyer, *Model Predictive Control of High Power Converters and Industrial Drives*. Hoboken, NJ, USA: Wiley, 2016.
[33] M. Cheng, R. Luo, and X. Wei, "Design and analysis of current control methods for brushless doubly-fed induction machines," *IEEE Trans. Ind. Electron.*, to be published. doi: 10.1109/TIE.2018.2829688.
[34] L. Shang and J. Hu, "Sliding-mode-based direct power control of grid-connected wind-turbine-driven doubly fed induction generators under unbalanced grid voltage conditions," *IEEE Trans. Energy Convers.*, vol. 27, no. 2, pp. 362–373, Jun. 2012.
[35] H. Nian, P. Cheng, and Z. Q. Zhu, "Coordinated direct power control of DFIG system without phase-locked loop under unbalanced grid voltage conditions," *IEEE Trans. Power Electron.*, vol. 31, no. 4, pp. 2905–2918, Apr. 2016.

Xinchi Wei (S'13) received the M.Sc. degree in control engineering from the Inner Mongolia University of Technology, China, in 2013. She is currently working toward the Ph.D. degree in electrical engineering at the Southeast University, Nanjing, China.

From June 2016 to June 2017, she was a joint Ph.D. student funded by China Scholarship Council with the School of Electrical, Mechanical and Mechatronic Systems, University of Technology Sydney, Australia. Her research interests include renewable energy systems, electrical machines, and power electronics.

Ming Cheng (M'01–SM'02–F'15) received the B.Sc. and M.Sc. degrees from Southeast University, Nanjing, China, in 1982 and 1987, respectively, and the Ph.D. degree from the University of Hong Kong, Hong Kong, in 2001, all in electrical engineering from.

Since 1987, he has been with Southeast University, where he is currently a Chair Professor in the School of Electrical Engineering and the Director of the Research Center for Wind Power Generation. His teaching and research interests include electrical machines, motor drives for electric vehicles, and renewable energy generation. He has authored or coauthored more than 380 technical papers and 4 books and is the holder of 100 patents in these areas.

Prof. Cheng is a Fellow of the Institution of Engineering and Technology. He has served as the Chair and Organizing Committee Member for many international conferences. He is a Distinguished Lecturer of the IEEE Industry Applications Society (IAS) in 2015/2016.

Jianguo Zhu (S'93–M'96–SM'03) received the B.E. degree in 1982 from the Jiangsu Institute of Technology, Jiangsu, China, the M.E. degree in 1987 from the Shanghai University of Technology, Shanghai, China, and the Ph.D. degree in 1995 from the University of Technology Sydney (UTS), Sydney, Australia, all in electrical engineering.

He was appointed a Lecturer at UTS in 1994 and promoted to Full Professor in 2004 and Distinguished Professor of Electrical Engineering in 2017. In 2018, he joined the University of Sydney, Australia, as a Full Professor and the Head of School of Electrical and Information Engineering. His research interests include computational electromagnetics, measurement and modeling of magnetic properties of materials, electrical machines and drives, power electronics, renewable energy systems, and smart micro grids.

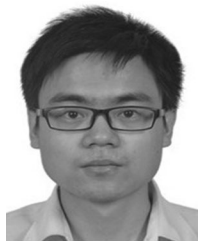

Haitao Yang (S'16) received the B.S. degree from the Hefei University of Technology, Hefei, China, in 2009, and the M.S. degree from the North China University of Technology, Beijing, China, in 2015, both in electrical engineering. He is currently working toward the Ph.D. degree in mechanical engineering at the School of Mechanical and Mechatronic Engineering, University of Technology, Sydney, NSW, Australia.

His research interests include motor drives, position/speed sensorless control of ac motors, PWM converters, and electric vehicles.

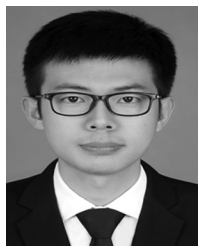

Rensong Luo received the B.Sc. and M.Sc. degrees in electrical engineering from Southeast University, Nanjing, China, in 2014 and 2017, respectively.

He is currently working in NR Electric Co. Ltd. His research interests include renewable energy systems and motor drives.